Active Control of an Acoustic Black Hole using a Feedback Strategy

K. Hook[a], S. Daley[a], J. Cheer[a,*]

[a]*Institute of Sound and Vibration Research, University of Southampton, Southampton, SO17 1BJ, Hampshire, UK*

Abstract

Acoustic black holes (ABHs) are tapered structural features that can achieve high levels of structural damping within lightweight constraints. It has previously been proposed to integrate feedforward active vibration control into an ABH to enable control over a broad spectrum, however, the time-advanced information required in this control strategy is not always available. In addition, it has been shown that controlling the reflection coefficient in a beam-based ABH leads to an undesirable enhancement of the taper vibration. In this paper, a feedback control strategy is applied to an ABH terminated beam, with a piezoelectric patch providing the control actuation. The feedback strategy is a remote vibration control methodology and is used to examine the different compensators that are potentially available to control simultaneously both the local taper vibration and the reflected wave component. The investigation highlights that the taper vibration can be minimised without affecting the reflected wave, however, apart from a few isolated frequencies, it is shown that the reflected wave cannot be minimised without increasing the taper vibration relative to the passive case. Importantly, since the approach enables the passive ABH performance to be maintained whilst simultaneously minimising the vibration in the tip, the fatigue life of the structure can potentially be extended with the addition of the active control loop.

Keywords: Acoustic Black Hole, Feedback, Active Control, Remote Damping

1. Introduction

An ABH can be realised as a smoothly varying structural feature that tapers from a thicker to a thinner profile [1]. The flexural wave speed in a beam can be related to the thickness of the structure and so as a flexural wave travels down the taper its speed is reduced, resulting in a low amount of reflected energy from the tip. In practice, a small amount of damping material is required to achieve good passive performance [2] and it has been shown that this damping material can be optimally placed to minimise vibration [3–5] or radiated sound [6]. The properties of the damping material can also be modified using temperature [7]. In addition to studies into the damping, there have been a variety of studies that examine different ways to tune the narrow and broadband performance of an ABH by varying the geometric design parameters, such as taper length, power law and tip height [3, 4, 8–14]. Different ABH constructions have also been examined such as rolling up a long taper to reduce the size of the ABH whilst maintaining good low frequency performance [15]. In addition to the passive tuning methods available, it has been proposed that active components could be used to enhance the performance of an ABH. The active ABH (AABH) can be realised using a number of different active control strategies in order to minimise different cost functions and this was demonstrated in the context of a feedforward wave-based control system in [16]. Although it was shown that the reflection coefficient could be effectively controlled, this control strategy resulted in a significant enhancement in the taper vibration which may accelerate damage due to structural fatigue. Additionally, this feedforward control strategy required time-advanced knowledge of the disturbance signal, something that is not always available in practical applications. A feedback approach may, therefore, provide a number of practical benefits. To provide further insight into the effect of wave control and to demonstrate a different and more compact approach to using an AABH, an investigation into the implementation of a feedback remote damping vibration controller [17] using a sensor and actuator pair located

*Corresponding Author
Email address: J.Cheer@soton.ac.uk (J. Cheer)

within the taper is presented in this paper. The approach, which was originally developed in [17], provides an explicit parameterisation of the design freedom available for any feedback compensator and so enables the tradeoff between minimising the local taper vibration and minimising the reflected wave component to be examined over a broad frequency range. The paper is organised as follows. The experimental setup used in this investigation and a brief overview of the wave decomposition method used to estimate the wave components in the structure are presented in Section 2. In addition, a controller is designed using the geometric approach from [17] and four control strategies are highlighted that can be used to control both the reflected wave component and the local taper vibration. Each compensator has initially been implemented in the frequency domain and the results are presented in Section 3. Following this, a recursive least squares tonal controller is presented in Section 4 that can be used to implement each compensator in the time domain and some examples are given. Finally, the conclusions of this work are presented in Section 5.

2. Controller Design

In this section, the controller design is presented for use on an active ABH termination. Initially, the experimental setup is described in Section 2.1 and the frequency responses of the system are presented. In Section 2.2, a remote damping controller that, when feasible, can simultaneously control the local taper vibration and the reflected wave component has been designed using the geometric approach described in [17].

2.1. Experimental Setup

Table 1 lists the dimensions of the experimental setup and a diagram of the setup is presented in Fig. 2. A photo of the setup is also shown in Fig. 1. The beam with the ABH has been manufactured out of T6 aluminium and the piezoelectric patch is a PI-876.A11 [18]. The primary disturbance, d, was used to drive a shaker with broadband white noise using a sampling frequency of 22 kHz. Accelerometers 1 and 2 were used to calculate the complex amplitude of the reflected wave component in the beam, ϕ^-, and accelerometer 3 was used to measure the local vibration in the taper. The control signal, u, was used to drive the piezoelectric transducer in order to control either the reflected wave component or the local taper vibration. Low-pass anti-aliasing and reconstruction filters with a cut-off frequency of 10 kHz were also used.

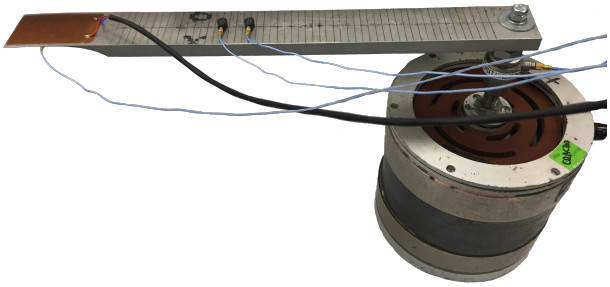

Figure 1: A photo showing the experimental setup.

Table 1: Dimensions of the experimental setup

Parameter	Value
Beam length	300 mm
Beam height	10 mm
Beam width	40 mm
ABH length	70 mm
ABH power law	4
ABH tip height	0.5 mm
Piezo length	61 mm
Piezo height	0.4 mm
Piezo width	35 mm
Piezo mass	4 g

The frequency responses measured at each of the locations can be written in terms of the contributions from the primary and secondary sources as [17]

$$\begin{Bmatrix} a_3(\omega) \\ \phi^-(\omega) \end{Bmatrix} = \begin{bmatrix} g_{11}(\omega) & g_{12}(\omega) \\ g_{21}(\omega) & g_{22}(\omega) \end{bmatrix} \begin{Bmatrix} u(\omega) \\ d(\omega) \end{Bmatrix}, \tag{1}$$

where g_{11} is the frequency response between the input voltage used to drive the piezoelectric transducer and the acceleration measured using the accelerometer on the taper, g_{12} is the frequency response between the input voltage used to drive the primary shaker and the acceleration measured using the accelerometer on the taper, g_{21} is the frequency

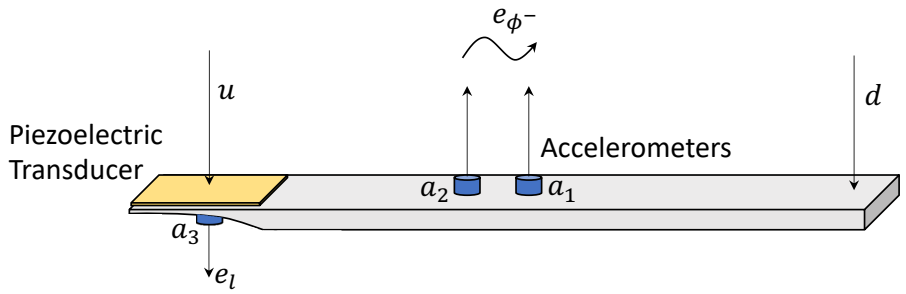

Figure 2: A diagram of an active ABH termination on one end of a beam. The primary disturbance is driven using the signal d, the control source is driven using the control signal u, the local error signal e_l is measured using accelerometer a_3 and the remote error signal e_{ϕ^-} is estimated using accelerometers a_1 and a_2.

response between the input voltage used to drive the piezoelectric transducer and the reflected wave component estimated using the accelerometers on the beam and g_{22} is the frequency response between the voltage used to drive the primary shaker and the reflected wave component estimated using the accelerometers on the beam. The control signal at any given frequency, u, can be calculated using the feedback control law,

$$u(\omega) = -\kappa(\omega)a_3(\omega). \tag{2}$$

Using a sampling frequency of 22 kHz, the primary responses between the disturbance signal used to drive the shaker and the three accelerometers were measured. The measurements were then repeated whilst driving the piezoelectric transducer to obtain the secondary responses. The primary and secondary frequency responses between the input voltages and the acceleration measured at each accelerometer were subsequently calculated using the H1-estimator. The frequency responses related to the accelerometers on the beam section were then used to estimate the frequency response of the reflected wave component using far-field wave decomposition.

In the frequency domain, the complex amplitudes of the incident and reflected wave components, $\phi^+(\omega)$ and $\phi^-(\omega)$, can be written in terms of the signal measured at the two accelerometers, a_1 and a_2, as

$$\begin{Bmatrix} a_1(\omega) \\ a_2(\omega) \end{Bmatrix} = -\omega^2 \begin{bmatrix} \mathrm{e}^{\mathrm{i}k\Delta/2} & \mathrm{e}^{-\mathrm{i}k\Delta/2} \\ \mathrm{e}^{-\mathrm{i}k\Delta/2} & \mathrm{e}^{\mathrm{i}k\Delta/2} \end{bmatrix} \begin{Bmatrix} \phi^+(\omega) \\ \phi^-(\omega) \end{Bmatrix}, \tag{3}$$

where ω is the angular frequency, k is the flexural wavenumber and Δ is the sensor separation [22, 23]. Eq. 3 can be rearranged to give

$$\begin{Bmatrix} \phi^+(\omega) \\ \phi^-(\omega) \end{Bmatrix} = -\frac{1}{\omega^2\left(\mathrm{e}^{\mathrm{i}k\Delta} - \mathrm{e}^{-\mathrm{i}k\Delta}\right)} \begin{bmatrix} \mathrm{e}^{\mathrm{i}k\frac{\Delta}{2}} & -\mathrm{e}^{-\mathrm{i}k\frac{\Delta}{2}} \\ -\mathrm{e}^{-\mathrm{i}k\frac{\Delta}{2}} & \mathrm{e}^{\mathrm{i}k\frac{\Delta}{2}} \end{bmatrix} \begin{Bmatrix} a_1(\omega) \\ a_2(\omega) \end{Bmatrix}, \tag{4}$$

which can be simplified to

$$\phi^+(\omega) = h_-(\omega)a_2(\omega) - h_+(\omega)a_1(\omega) \tag{5}$$

$$\phi^-(\omega) = h_-(\omega)a_1(\omega) - h_+(\omega)a_2(\omega), \tag{6}$$

where

$$h_+(\omega) = \frac{\mathrm{e}^{\mathrm{i}k\frac{\Delta}{2}}}{\omega^2\left(\mathrm{e}^{\mathrm{i}k\Delta} - \mathrm{e}^{-\mathrm{i}k\Delta}\right)}; \qquad h_-(\omega) = \frac{\mathrm{e}^{-\mathrm{i}k\frac{\Delta}{2}}}{\omega^2\left(\mathrm{e}^{\mathrm{i}k\Delta} - \mathrm{e}^{-\mathrm{i}k\Delta}\right)}. \tag{7}$$

In order to implement Eq. 5 and 6 in the time domain, $h_-(\omega)$ and $h_+(\omega)$ can be approximated using discrete-time FIR filters [22, 24, 25], which gives the vectors of filter coefficients $\boldsymbol{h}_-$ and $\boldsymbol{h}_+$ respectively. To ensure that the filters are causal, a small delay can be applied to the frequency responses prior to calculating the filters. Although effective, these wave decomposition filters are subjected to some limitations imposed by the sensor separation and sensor array location, which results in lower and upper frequency limits. In this investigation, the frequency range of interest has been limited to 400 Hz – 10 kHz and further information regarding the derivation of these limits can be found

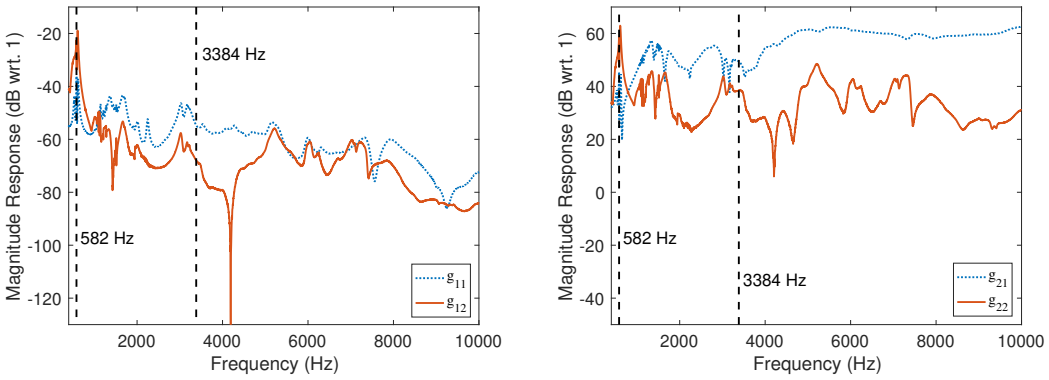

(a) (b)

Figure 3: (a) The local (local taper vibration) and (b) remote (reflected wave component) frequency responses. The primary responses are shown by the solid red lines and the secondary responses are shown by the dotted blue lines. Two frequencies have been highlighted by the black dashed lines and correspond to the examples given in Fig. 6.

in [22, 24, 25]. The resulting frequency responses for the local taper vibration and reflected wave component are presented over the selected frequency range in Fig. 3. From these frequency responses, it can be seen that for each set of responses there is a cross-over frequency where the secondary responses become higher than the primary responses, which is due to the better coupling between the piezoelectric patch and the structure at higher frequencies. For the local taper vibration this occurs at 1.1 kHz and for the reflected wave component this occurs at 800 Hz. It has been previously demonstrated in [16] that an AABH termination has a lower cross-over frequency compared to a constant thickness termination, which results in a comparatively lower energy input when implementing a control strategy.

2.2. Compensator Selection

A block diagram of the control system, corresponding to Fig. 2, is shown in Fig. 4. By substituting Eq. 2 into Eq. 1 and re-arranging, the local taper and reflected wave closed loop transfer functions can be written as

$$\frac{e_l(\omega)}{d(\omega)} = \frac{g_{12}(\omega)}{1 + g_{11}(\omega)\kappa(\omega)} \tag{8}$$

$$\frac{e_{\phi^-}(\omega)}{d(\omega)} = g_{22}(\omega) - \frac{\kappa(\omega)g_{12}(\omega)g_{21}(\omega)}{(1 + g_{11}(\omega)\kappa(\omega))}, \tag{9}$$

where the error term $e_l(\omega)$ represents the local frequency response measured at accelerometer a_3 and the error term $e_{\phi^-}(\omega)$ represents the reflected wave component frequency response $\phi^-(\omega)$. The frequency dependency is omitted from this point forward for clarity, but it should be assumed unless stated otherwise.

Following the approach presented in [17] the conditions required to control either the local taper acceleration or the reflected wave can be determined by rewriting the closed loop transfer functions as

$$\frac{e_l}{d} = f_l(\kappa)g_{12} \tag{10}$$

$$\frac{e_{\phi^-}}{d} = f_{\phi^-}(\kappa)g_{22}, \tag{11}$$

where

$$f_l(\kappa) = \frac{1}{1 + g_{11}\kappa} \tag{12}$$

$$f_{\phi^-}(\kappa) = 1 - \frac{\kappa g_{12}g_{21}}{g_{22}(1 + g_{11}\kappa)}. \tag{13}$$

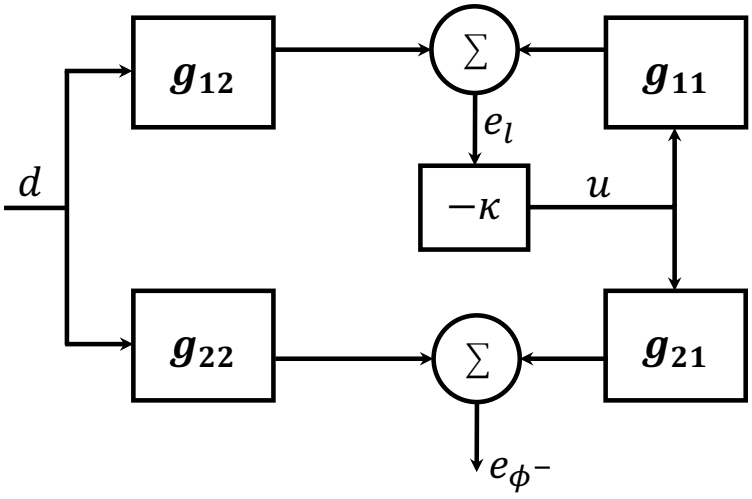

Figure 4: A block diagram showing the feedback control system. The local error signal is fed back through a compensator, κ, to obtain the control signal, u. The control signal is used to drive the piezoelectric transducer and the control of both the taper vibration and the reflected wave component can be examined.

It can be seen that if $\kappa = 0$, $f_l(\kappa)$ and $f_{\phi^-}(\kappa)$ become equal to 1 and Eq.s 10 and 11 become the open loop transfer functions for the local taper and reflected wave error respectively. To reduce both error signals relative to the uncontrolled case requires that the following conditions,

$$|f_l(\kappa)g_{12}| < |f_l(0)g_{12}| \tag{14}$$

$$\left|f_{\phi^-}(\kappa)g_{22}\right| < \left|f_{\phi^-}(0)g_{22}\right|, \tag{15}$$

or equivalently

$$\left|\frac{1}{1+g_{11}\kappa}\right| \; < \; 1 \tag{16}$$

$$\left|1-\frac{\kappa g_{12}g_{21}}{g_{22}(1+g_{11}\kappa)}\right| \; < \; 1, \tag{17}$$

are simultaneously satisfied. By defining the sensitivity function as α, inequality 16 can be simply stated as

$$|\alpha| < 1 \tag{18}$$

and the compensator expressed as

$$\kappa = \frac{(1-\alpha)}{\alpha g_{11}}. \tag{19}$$

As shown in [17], the sensitivity function can also be expressed in terms of a design freedom parameter γ as

$$\alpha = \gamma + 1 \tag{20}$$

so that inequality 16 becomes

$$|\gamma + 1| \; < \; 1 \tag{21}$$

and the compensator can then be expressed as

$$\kappa = \frac{-\gamma}{(1+\gamma)g_{11}}. \tag{22}$$

Inequality 17 can then be expressed in terms of the design parameter γ by substituting Eq 22 into Eq 17. The resulting inequality is

$$\left|1 + \frac{\gamma}{\tilde{g}}\right| < 1, \tag{23}$$

where

$$\tilde{g} = \frac{g_{11}g_{22}}{g_{12}g_{21}}. \tag{24}$$

Condition 21 describes the interior of a circle on the complex γ-plane with unity radius and centre point located at (-1,0), whilst condition 23 describes the interior of a circle on the complex γ-plane with $|\tilde{g}|$ radius and centre point located at $-\tilde{g}$. An example of the two circles for a specific frequency is shown in Fig. 5. The design process proceeds by selecting γ for a given frequency and calculating the respective compensator given by Eq. 22.

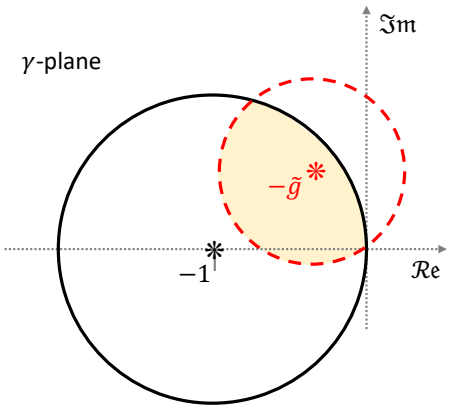

Figure 5: Mapping of the limit of inequality 23 onto the complex γ-plane. The black circle corresponds to the local error signal, the dashed red circle corresponds to the remote error signal and the yellow highlighted area where the circles intersect represents a simultaneous reduction in both error signals.

Referring to Fig. 5, the centre point of each of these circles corresponds to a point on the γ-plane that can be used to calculate a compensator that completely cancels, or annihilates the respective error signal. Alternatively, if a point on the γ-plane is selected from the edge of one of the circles, then this value can be used to calculate a compensator that neither attenuates nor enhances the error corresponding to that circle. Both circles will also intersect at the origin (0,0) of the γ-plane and by referring to Eq. 22 it can be seen that when γ is equal to zero, κ is equal to zero and there is subsequently no control. If, say, a point is chosen that falls within both circles, then a compensator can be calculated that reduces both the local and remote error. However, if a point is chosen from outside one of the circles then that error signal will be enhanced. It should be noted that due to the formulation of Eq. 22, annihilation of the local error is impractical because it requires an infinitely large gain. This could be solved by using, for example, an Instantaneous Harmonic Controller (IHC) architecture [17].

The controller design presented here is tonal, which means that for each frequency γ must be selected from the γ-plane in order to calculate κ. If this selection process is carried out over a broad range of frequencies, a vector of compensator values can be calculated that can be used to design a broadband controller. However, this process is not straightforward, since both the causality and stability of this broadband controller must be considered. The basic controller design process for the broadband case is explored in [17] and design procedures for minimum phase and non-minimum phase control path transfer functions (i.e. g_{11}) are detailed in [20] and [21] respectively.

To avoid predicting unrealistic levels of control, each compensator has been constrained by setting a lower limit of 0.1 for inequalities 21 and 23, such that

$$0.1 < |\gamma + 1| < 1 \tag{25}$$

$$0.1 < \left|1 + \frac{\gamma}{\tilde{g}}\right| < 1. \tag{26}$$

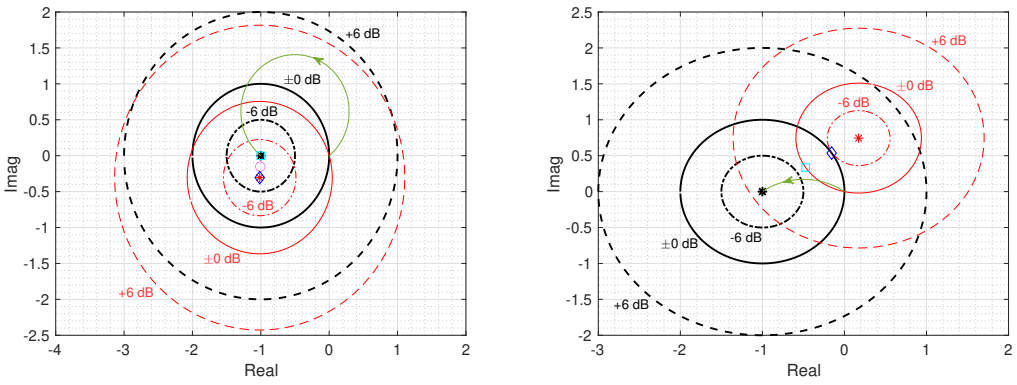

Figure 6: The thin red circle representing control of the reflected wave component plotted with respect to the thick black unit circle representing control of the local vibration at (a) 582 Hz and (b) 3384 Hz. The solid lines represent 0 dB of attenuation, the dash-dotted lines represent 6 dB of attenuation, the dashed lines represent 6 dB of enhancement and the asterisk represents minimisation of the respective quantity. The cyan square represents the best possible control of the local taper vibration without enhancing the reflected wave and the blue diamond represents the best possible control of the reflected wave without enhancing the local taper vibration. The magenta circle in (a) is the point that gives an equal reduction in both error signals. The green contours with arrows represent a velocity feedback system with an increasing gain in the direction of the arrow.

This constraint can be implemented by ensuring that the point on the γ-plane used to calculate a compensator does not lie within a factor of 0.1 of each circle's radius.

To demonstrate how a compensator can be selected from the controller design method presented above, two examples are given in Fig. 6 at 582 Hz (on resonance) and at 3384 Hz (off resonance). These have been marked on Figures 3(a) and 3(b) using black dashed lines. The results presented in Fig. 6 show a thick solid-lined black circle that has been plotted in the γ-plane using Eq. 21 and a thin solid-lined red circle that has been plotted by mapping Eq. 23 onto the γ-plane. The asterisks at the centre of each circle represent the minimisation of the respective error and the small blue diamond and cyan square represent the best control cases possible without enhancing either the local taper vibration or the reflected wave component. Finally, the dash-dotted lines represent 6 dB of attenuation and the dashed lines represent 6 dB of enhancement in the respective error signal.

In Fig. 6(a), it can be seen that the (-1,0) point that corresponds to minimisation of the local vibration lies within the -6 dB circle of control of the reflected wave. Therefore, at 582 Hz, minimising the local taper vibration will also attenuate the reflected wave, in this case by approximately 10 dB. Minimising the reflected wave component will also result in attenuation of the local taper vibration because the red asterisk lies within the -6 dB dash-dotted black line. At this frequency, either of the two errors can be minimised without enhancing the other and therefore the cyan square, that represents reducing the local taper vibration without enhancing the reflected wave, and the blue diamond, that represents reducing the reflected wave without enhancing the local taper vibration, are both located on the minimisation asterisks. The final control case highlighted in Fig. 6(a) is marked by a magenta circle. This point lies midway between the centres of both circles and can be used to calculate a compensator that equally controls the reflected wave component and the local taper vibration.

The results in Fig. 6(b) show a different set of circles for this control system, at a frequency where minimising either quantity will result in enhancement of the other. From these results it can be seen that a compensator that minimises the local taper vibration (from the (-1,0) point) will enhance the reflected wave component by approximately 5 dB, whilst a compensator that minimises the reflected wave component (from the $-\tilde{g}$ point) will enhance the local taper vibration by approximately 3 dB. At this frequency, it can be seen that the largest reduction in the local taper vibration that can be achieved without enhancing the reflected wave component will occur if a compensator is calculated using the point at (-0.5,0.3), which is highlighted by a cyan square. In this case, approximately 4 dB of attenuation is achieved in the local taper vibration without enhancing the reflected wave component. It can also be seen that if a compensator is calculated using the point (-0.2,0.5), highlighted by a blue diamond, then approximately

6 dB of attenuation can be achieved in the reflected wave component without enhancing the local taper vibration.

An advantage of this geometric design procedure is that different control strategies can be mapped onto the γ-plane to determine how they will affect each error signal. In this case, a green contour with an arrow has been added to each example to demonstrate how increasing the gain of a pure velocity feedback controller affects each error signal. At each frequency this contour has been calculated by expressing the compensator in terms of velocity,

$$\kappa = \frac{\kappa_v}{i\omega}. \tag{27}$$

Substituting Eq. 27 into Eq. 22 and rearranging for γ gives

$$\gamma_v = \frac{-g_{11}\kappa_v}{(i\omega + \kappa_v g_{11})}, \tag{28}$$

which can be plotted on the γ-plane for a range of gains. In each case, the contour starts at the origin, when $\kappa_v = 0$, and converges to the (-1,0) point as $\kappa_v \to \infty$. In Fig. 6(a), it can be seen that the pure velocity feedback contour does not fall between the two circle centre-points for any value of κ_v and a higher gain is required to achieve any reduction in the reflected wave component. In Fig. 6(b), the pure velocity feedback contour only falls between the circle centre-points when the gain is higher, however at this point the reflected wave component is enhanced. These results have shown that a pure velocity feedback controller is constrained to a particular contour on the γ-plane and, in this case, is not a suitable control strategy to achieve a reduction in both error signals.

3. Frequency domain performance

In this section the frequency responses are used to examine the tradeoff between minimising the local taper vibration and minimising the reflected wave component. Four control case studies are then selected and the corresponding compensator values are calculated. The compensators are implemented in the frequency domain and the relationship between controlling the reflected wave component and controlling the local taper vibration is explored.

Using the four control compensator selection criteria described previously, the compensator responses have been calculated over frequency and their performance can be seen in Fig. 7 over a bandwidth of 400 Hz to 10 kHz. In each case, the compensator has been calculated using Eq. 22, taking into account the performance constraints, 25 and 26, which limit the maximum attenuation to approximately 20 dB for clarity and avoid the prediction of unrealistic levels of control gain. From the results presented in Fig. 7, it can be seen that when control is set to minimise the local taper vibration (shown by the solid blue lines), the vibration in the taper is reduced by approximately 20 dB at all frequencies, which is simply limited by the constraints used in the study. The corresponding reflected wave component is generally unchanged, varying by approximately ± 1 dB over the bandwidth presented. However, there are specific frequencies and frequency bands that are attenuated or enhanced slightly more. For instance, at 582 Hz, the resonance frequency used as an example in Fig. 6(a), there is approximately 10 dB of attenuation, which is consistent with the prediction. Additionally, there is also a simultaneous reduction at 4198 Hz, which is very close in frequency to a large enhancement, as detailed below. The frequency bands 600 Hz – 1 kHz, 1.4 kHz – 1.8 kHz and 2.8 kHz – 4.5 kHz are enhanced by up to 30 dB. The largest of these enhancements occurs around 4190 Hz and, by referring back to Fig. 3(b), it can be seen that there is a strong anti-resonance in the primary response of the reflected wave component at this frequency. The enhancement in the reflected wave component occurs because, although minimising the vibration in the taper perfectly dampens the taper, this control strategy introduces a high impedance change at the ABH junction, which can be considered as a zero velocity boundary condition. This essentially truncates the termination at the ABH junction, making it equivalent to a flat termination. This study has shown that minimising vibration in the taper is not a suitable control strategy if the objective is to maintain or improve the damping performance of the ABH.

When control is set to minimise the reflected wave component (shown by the dash-dotted yellow lines), the results in Fig. 7 show that the reflected wave component is reduced by approximately 20 dB at all frequencies, which is again limited by constraints 25 and 26. It can be seen from the response in the taper, that this control strategy leads to a significant increase in the taper vibration of up to 30 dB. There are, however, three narrow frequency bands where the local vibration is reduced by up to 10 dB and these are around 582 Hz, 620 Hz and 4198 Hz. This control strategy is of particular interest because one of the key performance criteria of an ABH applied as a beam termination is its

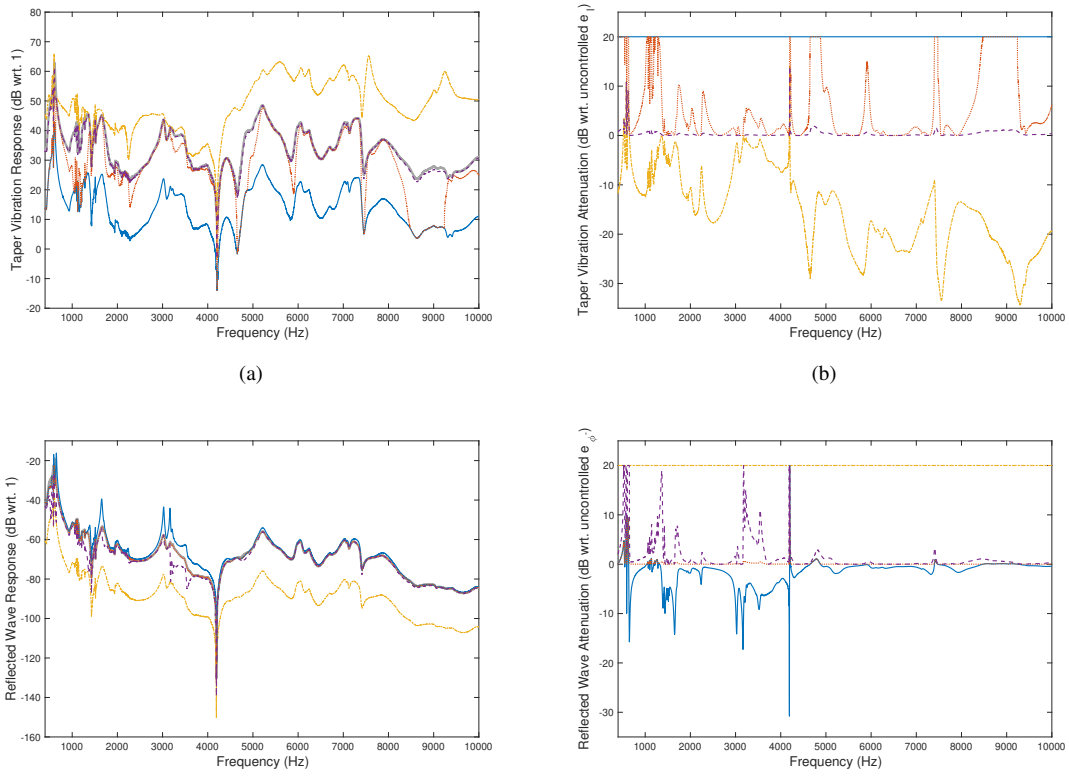

Figure 7: Feedback control implemented for the four cases and presented in terms of the responses (a, c) and attenuation (b, d). The effect that each compensator has in the local vibration is shown in (a, b) and the effect that each compensator has in the reflected wave is shown in (c, d). The uncontrolled case is represented by a thick grey line in (a, c) and 0 dB of attenuation in (b, d), the local minimisation case is represented by a solid blue line, the reflected wave minimisation case is represented by a dash-dotted yellow line, the local reduction without enhancement of the reflected wave case is represented by a dotted red line and the reflected wave reduction without enhancement of the local vibration is represented by a dashed purple line.

reflection coefficient. It has been previously shown that the reflection coefficient can be controlled using a feedforward control architecture in [16] and that this control strategy results in an enhancement in the taper response. This study demonstrates the same relationship between the reflection coefficient and the taper vibration amplitude.

In order to reduce effects of structural fatigue, the results from the two control strategies that focus on minimising the reflected wave without enhancing the level of vibration in the taper or, alternatively, minimising the local vibration in the taper without enhancing the reflected wave component have been presented. In the former case, the performance is shown by the dashed purple line in Fig. 7 and it can be seen that there are a number of narrow bandwidths where the reflected wave can be reduced by up to 20 dB (limited by the performance constraints) without enhancing the taper vibration. These narrow bandwidths can all be seen to occur below 5 kHz, except one small reduction at approximately 7.5 kHz. Although this control strategy is not particularly effective at higher frequencies, it should be noted that the uncontrolled ABH already provides a high level of damping and so high frequency vibrations are unlikely to cause issues in practice. When the latter control strategy is implemented to reduce the local taper vibration without enhancing the reflected wave component, it can be seen from the red dotted line in Fig. 7 that a reduction in the local vibration can be achieved over a number of frequency bands, covering the full bandwidth presented. In application, the choice of control strategy will depend on the nature of the problem and a combination of the different control strategies will likely produce the best solution to a broadband problem.

4. Time domain performance

In order to perform the time domain analysis, a recursive least squares (RLS) control architecture based on [19] is used here. FIR filters with 2 coefficients were used to model the frequency responses presented in Section 2.1 at each chosen frequency. These FIR filters were estimated using the MATLAB function `invfreqz`. A block diagram of the controller is shown in Fig. 8. In the block diagram shown, $e_l(n)$ is the n-th sample of the error signal, $z(n)$ is the n-th sample of an artificially generated reference signal and $u(n)$ is the control signal. $\hat{e}_l(\omega)$ is an estimate of the gain and phase of the error signal relative to the reference signal, which can be expressed as

$$\hat{e}_l(\omega) = \nu e^{i\phi}, \tag{29}$$

where ν is the gain relative to the reference and ϕ is the phase shift relative to the reference. In order to calculate $\hat{e}_l(\omega)$, the n-th sample of the error signal can be expressed as a sinusoidal tone relative to the reference,

$$e_l(n) = \nu \sin(\omega n T + \phi) + \epsilon(n), \tag{30}$$

where T is the sampling time period, ω is the angular frequency, and ϵ represents random white measurement noise with zero mean. Eq. 30 can be expanded as

$$e_l(n) = \nu \sin(\omega n T)\cos(\phi) + \cos(\omega n T)\sin(\phi) + \epsilon(n), \tag{31}$$

which is condensed to

$$e_l(n) = \theta(n)^T \mathbf{z}(n) + \epsilon(n), \tag{32}$$

where

$$\theta(n)^T = \begin{bmatrix} \nu\cos(\phi) & \nu\sin(\phi) \end{bmatrix} \tag{33}$$

is the vector containing the real and imaginary parts of the error signal with respect to the real and imaginary parts of the reference signal, which are contained within the vector

$$\mathbf{z}(n) = \begin{bmatrix} \sin(\omega_0 n T) & \cos(\omega_0 n T) \end{bmatrix}^T. \tag{34}$$

$\boldsymbol{\theta}_k$ can be estimated from the exponential forgetting RLS algorithm [26] as

$$\theta(n) = \theta(n-1) + \mathbf{K}(n)\left(e_l(n) - \theta(n-1)^T \mathbf{z}(n)\right), \tag{35}$$

where

$$\mathbf{K}(n) = \left(1 + \lambda^{-1}\mathbf{z}(n)^T \mathbf{P}(n-1)\mathbf{z}(n)\right)^{-1} \lambda^{-1}\mathbf{P}(n-1)\mathbf{z}(n) \tag{36}$$

and

$$\mathbf{P}(n) = \lambda^{-1}\mathbf{P}(n-1) + \lambda^{-1}\mathbf{K}(n)\mathbf{z}(n)^T \mathbf{P}(n-1). \tag{37}$$

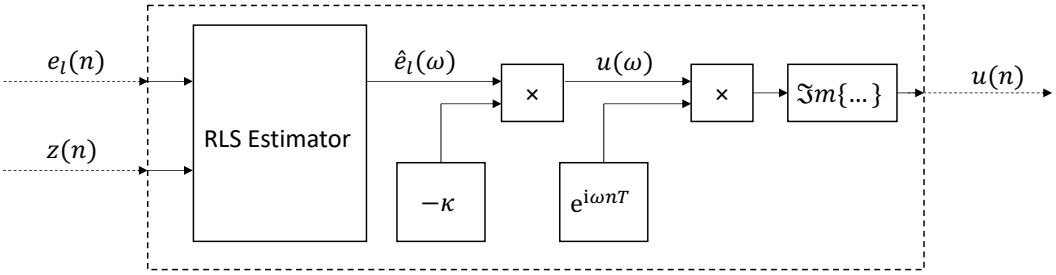

Figure 8: A block diagram showing the RLS based IHC. The inputs are the local error signal ($e_l(n)$) and a tonal reference signal (z), which are used to calculate the gain (ν) and phase (ϕ) of the tonal component of the error signal relative to the reference signal. The compensator (κ) is then applied in the frequency domain and the signal is transformed back into the time domain. The imaginary, sinusoidal, part of this signal is taken as the control signal.

The λ term in Equations 36 and 37 is a forgetting factor and takes a real value between 0 and 1. Although it is possible to implement the controller using a gradient descent method as shown in [19], in this study the compensator has been calculated earlier in this section and is implemented directly. An instantaneous inverse Fourier transform is then applied to the frequency domain control signal, $u(\omega)$, and the sinusoidal imaginary part of the subsequent signal is taken as the time domain control signal. Taking the feedback control law from Eq. 2 and the estimated error signal from Eq. 29, the time domain control signal [19] can be expressed as

$$u(n) = -\kappa v \sin(\omega n T + \phi). \tag{38}$$

The results presented in this section serve to demonstrate the performance of each of the control strategies in the time domain via simulation. The results are presented in terms of the AABH as a proof of concept and so no results for the standard beam are shown. The compensators used to obtain the results in Section 3 have been implemented at each frequency using the RLS based IHC architecture [19] described above. A pure sinusoidal tone was used as the disturbance signal. The two frequencies, 582 Hz and 3384 Hz, presented as an example in Figure 6 have been used to demonstrate each of the compensators in the time domain. The local taper vibration and reflected wave component error signals are shown before and after control, which has been turned on at t = 1 s, in Fig. 9 for each of the cases. The error signal has been normalised so that the pre-control level is ± 1 in each case to improve the clarity of the results. Each factor of 2 represents an increase or decrease of 6 dB in the error signal. For each case, Table 2 shows the increase or decrease in the error signal in decibels relative to the respective uncontrolled level.

Frequency	Control Case	Error	Level Change
3384 Hz	Local Minimisation	e_l	-20 dB
		e_{ϕ^-}	+5 dB
3384 Hz	Local Reduction Without	e_l	-4 dB
	Enhancing ϕ^-	e_{ϕ^-}	±0 dB
3384 Hz	ϕ^- Minimisation	e_l	+3 dB
		e_{ϕ^-}	-20 dB
3384 Hz	ϕ^- Reduction Without	e_l	±0 dB
	Enhancing Local Vibration	e_{ϕ^-}	-6 dB
582 Hz	Simultaneous Reduction	e_l	-15 dB
		e_{ϕ^-}	-15 dB

Table 2: The change in the local and reflected wave component (ϕ^-) error signals before and after control.

From the results shown in Fig. 9(a) and Table 2, it can be seen that at 3384 Hz the local taper vibration can be reduced by 20 dB, which causes a 5 dB enhancement of the reflected wave component. These levels are consistent with the frequency domain results shown in Section 3. The results in Fig. 9(b) and Table 2 show that approximately 4 dB of attenuation can be achieved in the local taper vibration without enhancing the reflected wave component. These results are also consistent with the frequency domain simulation results presented in Section 3. If, instead, the reflected wave component is minimised then from the results shown in Fig. 9(c) it can be seen that there is an enhancement in the local taper vibration. Referring to Table 2, it can be seen that this enhancement is 3 dB. If it is ensured that there is no enhancement in the local taper vibration, the controller can achieve approximately 6 dB of attenuation in the reflected wave component, which is shown both in Table 2 and in Fig. 9(d). Examining the implementation of control at 582 Hz, it was shown in Sections 2.2 and 3 that simultaneous reduction could be achieved in both the local taper vibration and the reflected wave component. To demonstrate this, a compensator has been calculated from the midpoint on the γ-plane between the two circles, which was highlighted by the magenta circle in Fig. 6(a). Implementing this compensator in the time domain gives the results presented in Fig. 9(e), which show the simultaneous reduction in both error signals. Referring to Table 2, it can be seen that each error signal is attenuated by approximately 15 dB. This specific case was not presented in the frequency domain implementation, however, the results are very similar to those obtained by implementing the compensators that minimise each error signal and so are considered consistent.

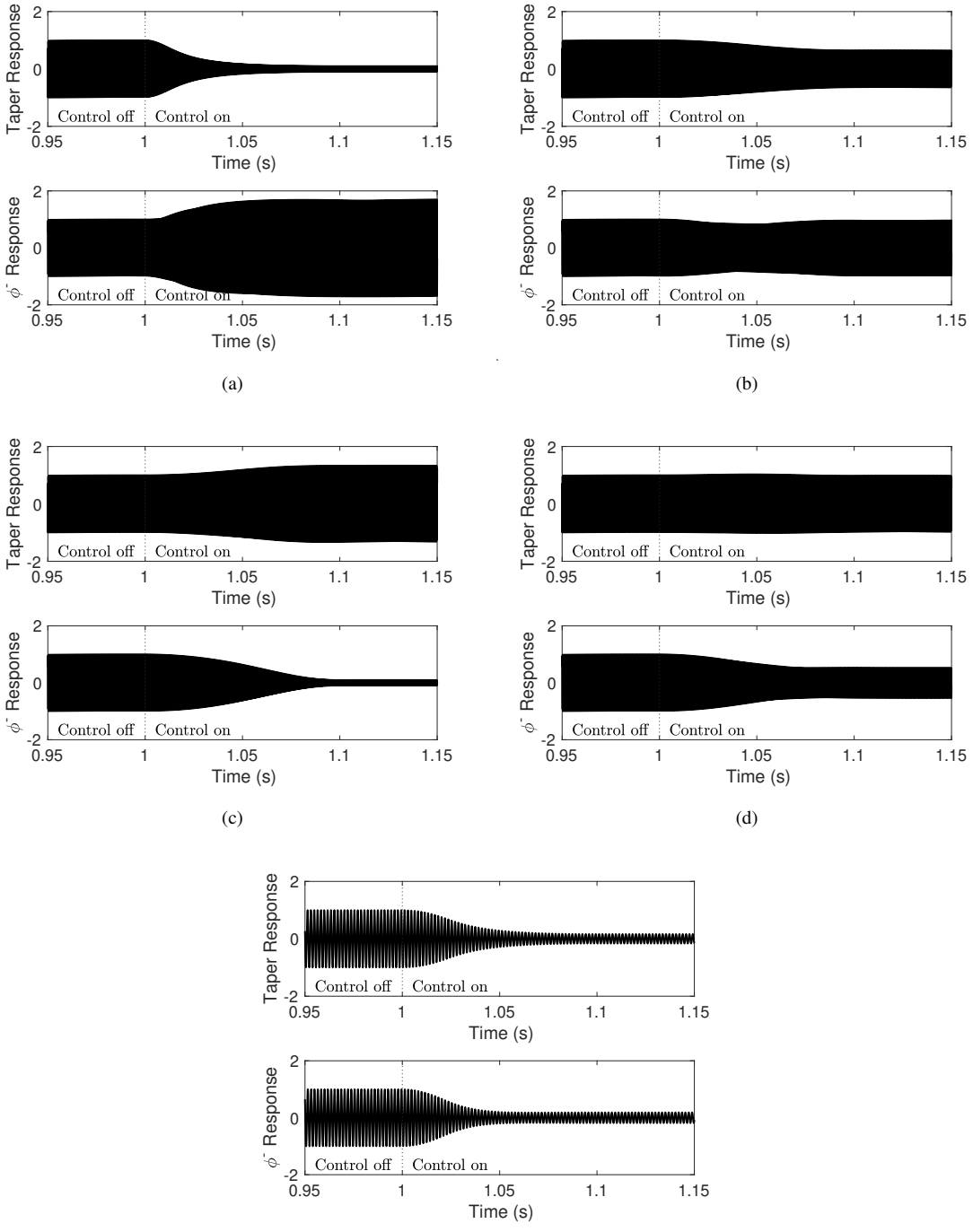

Figure 9: The local and remote error signals for each of the time domain cases, normalised with respect to the pre-control level. The frequencies and cases are (a) 3384 Hz Local Minimisation, (b) 3384 Hz Local Control, (c) 3384 Hz Remote Minimisation, (d) 3384 Hz Remote Control and (e) 582 Hz Simultaneous Control.

5. Conclusions

An investigation into the use of feedback control in an AABH has been presented in this paper. A geometric controller design for remote damping control has been used to examine the tradeoff between controlling the local taper vibration and controlling the reflected wave component. Four different control cases were chosen at each frequency and a compensator was calculated for each. A frequency domain implementation has shown that minimising the local taper vibration produces a small amount of unwanted enhancement in the reflected wave at frequencies below 5 kHz. Intuitively, minimising the taper vibration imposes a zero velocity boundary condition at the ABH junction, which can therefore be approximated as a constant thickness flat termination. Through further investigation, it has been shown that a control strategy such as pure velocity feedback control does not have any significant performance benefits, except perhaps at one or two very specific frequencies, and an alternative controller is required. It has also been shown that if the reflected wave component is minimised, similarly to the feedforward control strategy presented in [16], the local vibration in the taper is greatly enhanced. Although this leads to an improvement in ABH performance in terms of a low reflection coefficient, the subsequent enhancement of vibration in the thin region of the taper may lead to early failure due to increased structural fatigue. In addition, designing a stable and robust feedback controller that greatly enhances the local vibration may be difficult. If a constraint is set so that the reflected wave is controlled without enhancing the taper vibration, it has been shown that some level of reduction in the reflected wave can be achieved below 5 kHz, but control above this frequency is very limited. There are only two narrow frequency bands where a simultaneous reduction of the reflected wave and taper vibration is possible in the considered case. It should be noted that one of these frequencies is a beam resonance and so this control strategy may be effective for controlling structurally radiated sound. If a constraint is set so that the taper vibration is controlled without enhancing the reflected wave, a reduction in the local taper vibration is achievable across a significant number of frequency bands across the full 400 Hz – 10 kHz bandwidth presented, including resonances. This control strategy may, therefore, be useful in applications where the ABH provides enough damping passively but is prone to fatigue due to high amplitude vibration in the taper. These final two control strategies have shown that a controller can be designed for applications where there are constraints on the performance or maximum vibration level. Finally, a time domain study has shown that an RLS based IHC can be used to implement each of the compensators effectively in the time domain and the results shown were consistent with the results from the frequency domain implementation.

Acknowledgements

This work was supported by an EPSRC iCASE studentship (Voucher number 16000058) and the Intelligent Structures for Low Noise Environments EPSRC Prosperity Partnership (EP/S03661X/1).

References

[1] M. Mironov, Propagation of a flexural wave in a plate whose thickness decreases smoothly to zero in a finite interval, Soviet Physics: Acoustics 34 (3) (1988), 318–319.

[2] V.V. Krylov, and F. Tilman, Acoustic 'black holes' for flexural waves as effective vibration dampers, Journal of Sound and Vibration 274 (2004), 605–619.

[3] L. Tang, L. Cheng, H. Ji, and J. Qiu, Characterization of acoustic black hole effect using a one-dimensional fully-coupled and wavelet-decomposed semi-analytical model, Journal of Sound and Vibration 374 (2016), 172–184.

[4] V.B. Georgiev, J. Cuenca, F. Gautier, L. Simon and V.V. Krylov, Damping of structural vibrations in beams and elliptical plates using the acoustic black hole effect, Journal of Sound and Vibration 330 (11) (2011), 2497–2508.

[5] E.P. Bowyer, D.J. O'Boy, V.V. Krylov and J.L. Horner, Effect of geometrical and material imperfections on damping flexural vibrations in plates with attached wedges of power law profile, Applied Acoustics 73 (2012), 514–523.

[6] L. Ma and L. Cheng, Topological optimization of damping layout for minimized sound radiation of an acoustic black hole plate, Journal of Sound and Vibration 458 (2019), 349–364.

[7] M. Ouisse, D. Renault, P. Butaud and E. Sadoulet-Reboul, Damping control for improvement of acoustic black hole effect, Journal of Sound and Vibration 454 (2019), 63–72.

[8] K. Hook, J. Cheer and S. Daley, A Parametric Study of an Acoustic Black Hole on a Beam, The Journal of the Acoustical Society of America 145 (6) (2019), 3488–3498.

[9] D.J. O'Boy, V.V. Krylov and V. Kralovic, Damping of flexural vibrations in rectangular plates using the acoustic black hole effect, Journal of Sound and Vibration 329 (22) (2010), 4672–4688.

[10] C.A. McCormick and M.R. Shepherd, Optimal design and position of an embedded one-dimensional acoustic black hole, in: Proceedings of Inter-Noise 2018, Chicago, IL, USA, (2018), 26–29.

[11] C.A. McCormick and M.R. Shepherd, Design optimization and performance comparison of three styles of one-dimensional acoustic black hole vibration absorbers, Journal of Sound and Vibration 420 (2020), 1–12.
[12] V. Denis, A. Pelat, F. Gautier and B. Elie, Modal overlap factor of a beam with an ABH termination, Journal of Sound and Vibration 333 (12) (2014), 2475–2488.
[13] A. Karlos, S.J. Elliott and J. Cheer, Higher-order WKB analysis of reflection from tapered elastic wedges, Journal of Sound and Vibration 449 (2019), 368–388.
[14] P.A. Feurtado and S.C. Conlon, Investigation of boundary-taper reflection for acoustic black hole design, Journal of Noise Control Engineering 5 (2015), 460–466.
[15] J.Y. Lee and W. Jeon, Vibration damping using a spiral acoustic black hole, The Journal of the Acoustical Society of America 141 (3) (2017), 1437–1445.
[16] J. Cheer, K. Hook and S. Daley, Active feedforward control of flexural waves in an Acoustic Black Hole terminated beam, Smart Materials and Structures 30 (3) (2021), 1–14.
[17] S. Daley and J. Wang, A geometric approach to the design of remotely located vibration control systems, Journal of Sound and Vibration 318 (2008), 702–714.
[18] PI Ceramic, PI876.A11 piezo patch, `https://static.piceramic.com/fileadmin/user_upload/physik_instrumente/files/datasheets/P-876-Datasheet.pdf`, 2021 (accessed 10 June 2021).
[19] S. Daley and I. Zazas, A recursive least squares based control algorithm for the suppression of tonal disturbances, Journal of Sound and Vibration 331 (2012), 1270–1290.
[20] J. Wang and S. Daley, Broad band controller design for remote vibration using a geometric approach, Journal of Sound and Vibration 329 (2010), 3888–3897.
[21] U. Ubaid, S. Daley, S.A. Pope and I. Zazas, Design of stable and broadband remote vibration controllers for systems with local nonminimum phase dynamics, IEEE Transactions on control systems technology 24 (2) (2016), 654–661.
[22] E. Rustighi, B.R. Mace and N.S. Ferguson, An adaptive anechoic termination for active vibration control, Journal of Vibration and Control 17 (13) (2011), 2066–2078.
[23] C.R. Fuller, S.J. Elliott and P.A. Nelson, Active Control of Vibration, Academic Press, London, 1996.
[24] C.R. Halkyard and B.R. Mace, Feedforward adaptive control of flexural vibration in a beam using wave amplitudes, Journal of Sound and Vibration 254 (1) (2002), 117–141.
[25] B.R. Mace and C.R. Halkyard, Time domain estimation of response and intensity in beams using wave decomposition and reconstruction, Journal of Sound and Vibration 230 (3) (2000), 561–589.
[26] L. Ljung, Recursive identification algorithms, Circuits, Systems and Signal Processing 21 (1) (2002), 57–68.